Assessing Reaction Mechanisms of Graphite Negative Electrodes Based on *Operando* Synchrotron Radiation Diffraction Data

Journal of The Electrochemical Society, 2021 **168** 040509

Assessing Reaction Mechanisms of Graphite Negative Electrodes Based on *Operando* Synchrotron Radiation Diffraction Data

Hiroyuki Fujimoto,[1,z] Hisao Kiuchi,[1] Shigeharu Takagi,[1] Keiji Shimoda,[1] Ken-ichi Okazaki,[1] Zempachi Ogumi,[1,*] and Takeshi Abe[2,]**

[1]*Office of Society-Academia Collaboration for Innovation, Kyoto University, Kyoto 611-0011, Japan*
[2]*Graduate School of Global Environmental Studies, Kyoto University, Kyoto 615-8510, Japan*

Since the commercialization of rechargeable Li ion batteries in the early 1990 s, the performance of these devices has continually improved. In such batteries, graphite is typically used as the negative electrode and the present work examined the reaction mechanisms at graphite negative electrodes based on *operando* synchrotron X-ray diffraction analyses during charge/discharge. The resulting in-plane diffraction patterns of the Li-intercalated graphite permitted a detailed analysis of changes in the three-dimensional structure of the electrode. As the intercalation proceeded from a dilute stage 1 (with less Li intercalation) to a final stage 1 (the formation of LiC_6), the material transitioned from a random in-plane structure to a p($\sqrt{3} \times \sqrt{3}$)R30° in-plane structure via a superlattice based on a p(3 × 3)R0° in-plane structure. The data also indicate that a series of superlattices was formed during the reaction of the electrode as a result of successive rearrangements, depending on the amount of Li intercalated into the graphite.
 [DOI: 10.1149/1945-7111/abf181]

Manuscript submitted February 4, 2021; revised manuscript received March 10, 2021. Published April 6, 2021.

Despite the fact that the Li-ion battery is widely used throughout the world, there are many unsolved questions regarding its charge/discharge reaction. The fundamental reaction mechanism of the battery's negative electrode is considered to be the formation of a Li-graphite intercalation compound (Li-GIC). Initially, Li ions intercalate every few layers into graphite to form a higher stage structure. Finally (when fully intercalated, i.e. Li ions are inserted between all layers) the stage 1 structure is formed via stages 3 and 2. The structures of the stage 1 and 2 compounds have been investigated in detail.[1–6] The former has the space group P6/mmm with a_0 = 0.4305 nm and c_0 = 0.3706 nm, while the latter has the space group P6/mmm with a_0 = 0.4288 nm and c_0 = 0.7063 nm. Both have the same in-plane structure defined by p($\sqrt{3} \times \sqrt{3}$)R30° (as shown in Fig. A·1), where p denotes a primitive unit cell, ($i \times j$) denotes the unit vectors in units of a_0 = 0.24612 nm in the hexagonal lattice primitive cell, and Rθ denotes the angle of rotation of the unit vectors of the lattice relative to the graphite unit vectors.[4,5] The stoichiometry of the stage 1 compound has been confirmed as LiC_6 but that of the stage 2 compound is not yet certain. Guerard et al. determined a carbon/lithium atomic ratio between 11.84 and 25.22,[2,3] while Basu et al. reported values between 14.5 and 18.3.[7] Billaud prepared several Li-GICs at different stages and indexed the 00*l* diffractions of stages 1 to 5.[8] On this basis, they proposed another type of stage 2 compound (LiC_{18}) that has the in-plane structure p(3 × 3)R0° (In-plane composition with LiC_9).[8,9] Guerard et al. and Pfluger et al. also reported compounds for stages 5 and 6, respectively.[10] Dahn performed a comprehensive analysis of Li-GICs in graphite negative electrodes.[11] This work demonstrated that Li^+ ions were intercalated between all the graphite interlayers during the very initial stage of charging to form a dilute stage 1 compound that had a different stoichiometry from that of a conventional stage 1 compound. Dahn also found that, upon increases in the extent of Li^+ insertion, the Li-GIC structures transitioned in the order of dilute stage 1, stages 4 and 3, liquid-type stage 2 l and finally LiC_6-type stages 2 and 1, with no evidence of stages higher than stage 5. A number of researchers have cited and discussed this prior work,[12–15] although Dahn's paper does not provide information regarding the in-plane structure of LiC_9 or stages 5 and 6. Some reports, such as those of Billaud et al. and Guerard et al., have indicated observations of LiC_9 and stages 5 and 6. In addition, Ohzuku reported that the maximum stage in an LIB was stage 8, having a LiC_9 in-plane structure.[16] Zaghib et al. also reported the appearance of a stage 8 compound with the formula LiC_{72} based on ^{7}Li-NMR spectra.[17] Letellier and Chevallier employed ^{7}Li-NMR and proposed the formation of LiC_{6n} and LiC_{9n} structures.[14,15] On the other hand, Krachkovskiy et al. and Freytag et al. observed the signal of dilute stage structures by ^{7}Li-NMR.[18,19] Schweidler et al. proposed the solid solution (liquid type) stage structures by Rietveld analysis.[20] It is vital to assess the structures and reaction mechanisms associated with the formation of these higher stage compounds having LiC_9-type in-plane structures, so as to understand Li-GIC formation pathway and the dynamics. Uncertainty regarding the higher stage Li-GIC compounds has resulted from the inability to date to obtain clear X-ray diffraction (XRD) patterns of these low lithium concentration materials. The diffraction patterns acquired from Li-GICs using conventional laboratory XRD instruments provide only limited information concerning the structure along the *a*, *b*-axes and so the formation of LiC_9 has not been confirmed. However, new techniques have recently been employed such as the neutron diffraction and synchrotron X-ray diffraction (SXD) combined with 2D detector system to elucidate the detailed reaction mechanisms associated with Li-GICs during charge and discharge,[21–33] and some reports focused on the in-plane structural changes of Li-GICs.[22,31,32] In the present work, we investigated the intercalation mechanism of Li into graphite by *operando* analysis using SXD and elucidate the in-plane superlattice structures formed during intercalation/deintercalation.

Experimental

Procedure for the cell assembly.—As a starting material for the *operando* analysis, natural graphite (OMAC-R 1.0Z with median diameter of 18 μm, Osaka Gas Chemical Co., Ltd.) was used. An Al-laminated half-cell with the size of 70 × 70 mm composed of graphite and Li electrodes (25 × 25 mm) was assembled with an electrolyte of 1 mol·dm^{-3}-$LiPF_6$/ethylene carbonate + ethyl methyl carbonate (3:7) (Kishida Chemical Co., Ltd.). (Fig. 1) Because Li metal was used as a counter electrode, the graphite electrode was positive in the cell system. However, "charge" was defined as the intercalation into graphite and as "discharge" the Li deintercalation for the sake of consistency with a practical full-cell type rechargeable Li-ion battery. The cell was charged and discharged in advance before the *operando* measurement with a current of 0.1C (10 h) in the potential range of 0.01 V to 2.5 V. From the obtained charge/discharge curves, the differential *V*-d*Q*/d*V* curves were calculated.

*Electrochemical Society Fellow.
**Electrochemical Society Member.
[z]E-mail: fujimoto.hiroyuki.5n@kyoto-u.ac.jp

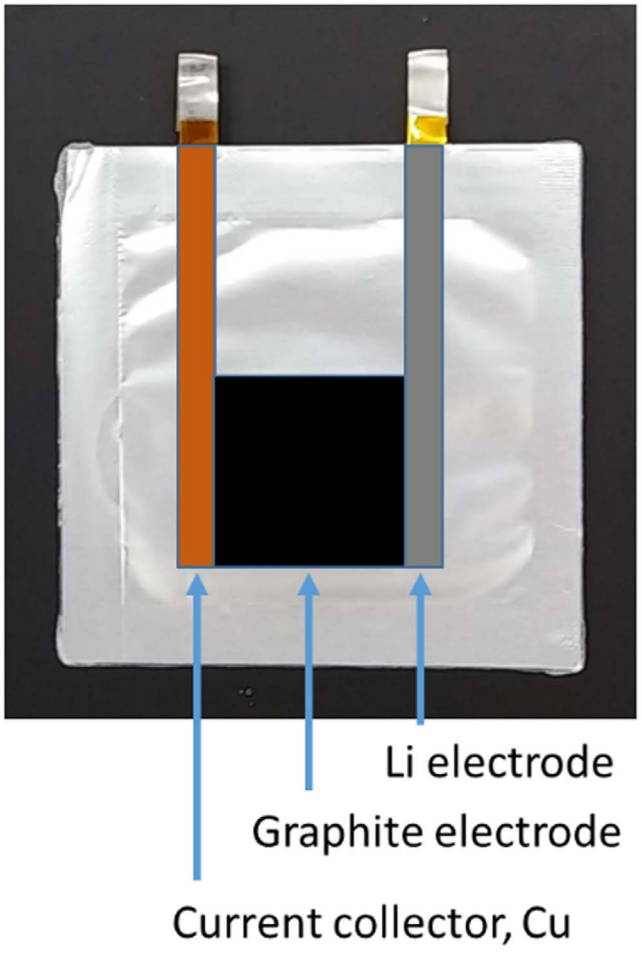

Figure 1. Laminated cell used in the present research.

Procedure for the SXD measurement.—The SXD measurements were performed during the second charge/discharge cycle at BL28XU in Super Photon ring-8 (SPring-8), Japan. The wavelength and size of the monochromatic X-ray beams were 0.04959 ± 0.00001 nm and 0.5 mm (horizontal) × 0.2 mm (vertical), respectively. The wavelength was calibrated by a CeO_2 reference XRD peaks (111, 220, and 200) in the reflection geometry. The operando measurement was performed in the transmission geometry using Si-based 2D pixel array detector (PILATUS 100 K, Rigaku Corporation) by setting the fixed angle, 2θ at 10.7°, which can measure the diffraction in Bragg's d value range from 0.17623 nm to 0.41347 nm at the same time, i.e. a greatly shortened data acquisition time. The reproducibility of diffraction peaks due to the position stability of the 2D detector was less than 0.00002 nm when integrated for 10 s, which is sufficient to track the change in d value due to operand measurement. Since the obtained XRD dataset were 2D image data, all the dataset recorded were converted to one-dimensional dataset composed of angle and intensity in order to estimate the d values. The intensity of incident beam was adjusted using Al attenuator, so that the Li-GIC did not decompose during the measurement by the strong beam. *Operando* measurement was repeated with exposure time of 10 s and measurement interval of 2 milliseconds, and 7200 SXD profiles were obtained during the charge/discharge process.

Procedure for the analysis of operando SXD data.—It was not possible to analyze such an enormous dataset of 7200 profiles manually. Hence, the analysis software "GIC Profile Chaser" was newly developed in Windows 10 (Fig. 2). The software enables us to track the profile changes of the 002, 100 and 101 peaks of graphite synchronizing with the charge/discharge curves, their differential curves (V-dQ/dV) and the compositions of LiC_x calculated from the charge/discharge curves and their cumulative Coulomb amount. First, from the changes in the profile of the 002 peak, it is possible to capture the various stages of structure change. Second, the formation process of the in-plane structure can be captured from the 100 peak change. Third, the transition point of the AB stacking ↔ AA stacking sequence can be determined from the 101 peak change. Using this software, all the

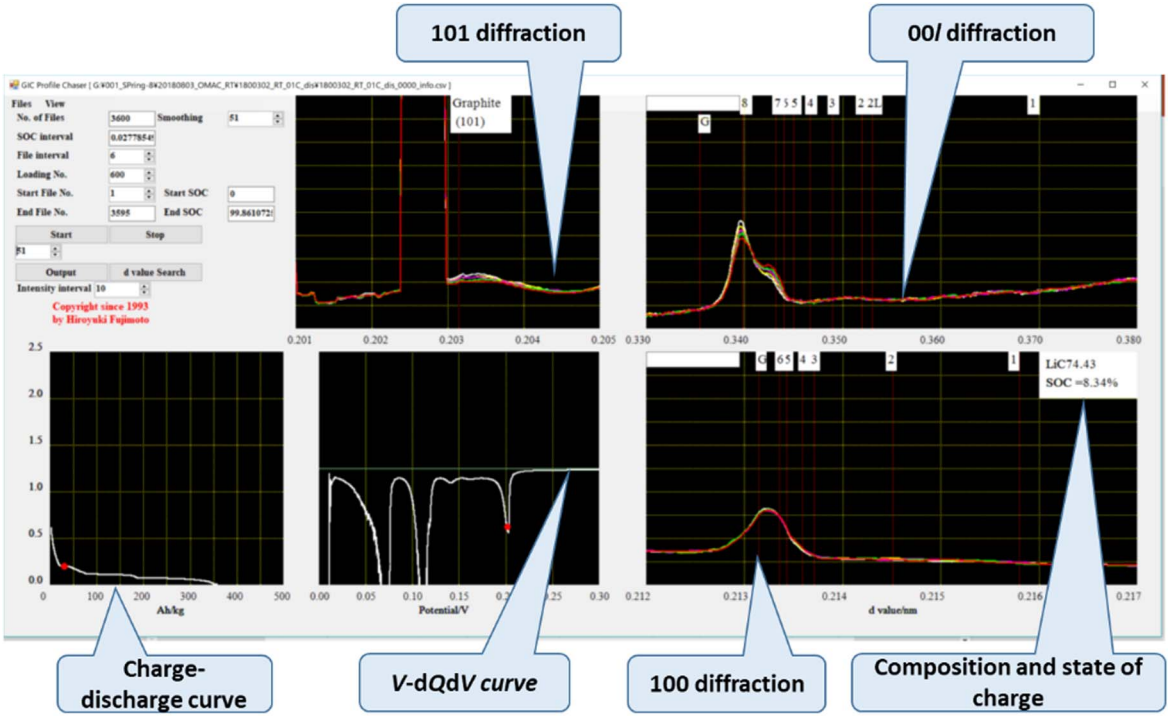

Figure 2. GIC Profile Chaser user interface.

diffractions during the charge/discharge processes were uploaded automatically to the computer. The profiles were successively displayed on a monitor as a series of diffraction profiles in conjunction with the compositions estimated from the charge/discharge curves, so that the profile change could be visually tracked on the monitor.

Results and Discussion

Factors affecting the stage changes of LiCx.—Figure 3 shows the changes in the patterns based on the 100 and 002 peaks of graphite negative electrodes during the charge/discharge process, as acquired at 1% state of charge (SOC) intervals at a charging rate of 0.1C. It is evident that well defined patterns were obtained that illustrate variations in the in-plane structure together with *c*-axis changes. The variations in the graphite 002 peaks are in agreement with previously reported data.[2–6] It is also apparent that the clear 100 in-plane profiles (that are difficult to obtain using standard laboratory XRD instrumentation) are highly correlated with the changes in the 002 pattern (that is, changes along the *c*-axis). Note that, in this figure, the 002 line of the stage 2 l compounds (d = ca. 0.352 nm), which was first reported by Dahn,[11] is observed only during the deintercalation process. That is, there is evident hysteresis between the intercalation and deintercalation. The changes in the Bragg's d values associated with the 100 and 002 peaks of the graphite were estimated from the overall patterns in Fig. 3 and are plotted in Fig. 4, which more clearly shows the hysteresis effect. Yazami et al. reported a similar hysteresis phenomenon in XRD data.[13] During the intercalation process, the d_{002} values undergo significant inflections or jumps at LiC_x x values of 108, 72, 54, 21 and 12, while the d_{100} values change at x = 72, 36, 27 and 21. Similarly, during the deintercalation, the d_{002} values exhibit inflections or jumps at x = 27, 36, 54, 72 and 216 and the d_{100} values change at x = 27 and 72. These inflections and jumps do not always have the same degree of sharpness during charge and discharge, which also suggests some hysteresis. All these compositions other than x = 21 can be assigned to LiC_{6n}, LiC_{9n} and LiC_{72n} compounds. The first two of these Li-GIC series were previously reported by Billaud, Ohzuku, Zaghib and Letellier et al.[8,14–17] However, the third series (LiC_{72n}), which includes compounds such as LiC_{72} and LiC_{216}, has not been previously reported. The charge curve in Fig. 5A also shows inflections at x = 108, 54, 36, 27 and 12, while the plot of the differential (V-dQ/dV) in Fig. 5B contains inflections between peaks corresponding to x = 108, 45, 36, 30, 27 and 12. Among these, the inflections and peaks corresponding to x = 108, 72, 63 and 54 are difficult to isolate because the potentials of these Li-GIC compounds are close to one another or the structures of these compositions are too flexible. The peak in the V-dQ/dV plot at approximately 0.2 V is believed to be associated with structures corresponding to x = 72, 63 and 54. It is widely accepted that LiC_6 (a stage 1 li-GIC) has a p($\sqrt{3} \times \sqrt{3}$)R30° structure. Combining the information concerning the d_{002} and d_{100} peaks, the stage 2 li-GIC appears to have two structures: p($\sqrt{3} \times \sqrt{3}$)R30° (LiC_{12}) and p(3 × 3)R0° (LiC_{18}). Both of the intercalation and deintercalation d_{100} data sets in Fig. 4 provide strong support for the existence of two stage 2 li-GIC compounds. However, the border of the in-plane transition between the p($\sqrt{3} \times \sqrt{3}$)R30° (LiC_{12}) and p(3 × 3)R0° (LiC_{18}) structures is vague. During intercalation, the p($\sqrt{3} \times \sqrt{3}$)R30° (LiC_{12}) compound appears close to LiC_{21}, while during deintercalation the structure remains unchanged up to LiC_{27} (see d_{100} = 0.2145 in Fig. 4). These results suggest that the in-plane transition from p(3 × 3)R0° to p($\sqrt{3} \times \sqrt{3}$)R30° is slower than the reverse transition from p(3 × 3)R0° to p($\sqrt{3} \times \sqrt{3}$)R30°. It should also be noted that the d_{002} value expands from 0.3513 nm to 0.3524 nm by 0.3% in the vicinity of LiC_{17} during deintercalation; this phenomenon is believed to be related to the in-plane transition from p($\sqrt{3} \times \sqrt{3}$)R30° to p(3 × 3)R0°. The present *operando* SXD analyses provide the first-ever clear evidence for this expansion. A unit cell expansion is typically endothermic, and the source of the energy required for this expansion is not yet clear, although we are currently attempting to determine the motive force based on theoretical calculations. If the in-plane structures of the higher stages are assumed to be based on p(3 × 3)R0° type super lattice, the observed compositions of the LiC_x (x = 18, 27, 36, 45, 54, 63 and 72) are reasonable. The peaks observed in the V-dQ/dV curves and the inflections in the charge curves in Fig. 5 can be explained as the result of transitions from stages 8 to stages 7, 6 and 5 (labelled I), stage 5 to stage 4 (II), stage 4 to stage 3 (III), stage 3 to stage 2 (IV), and stage 2 to stage 1 (V). It should also be noted that the higher stage Li-GICs such as LiC_{108} and LiC_{216} were difficult to assess, because these compounds generated weak signals.

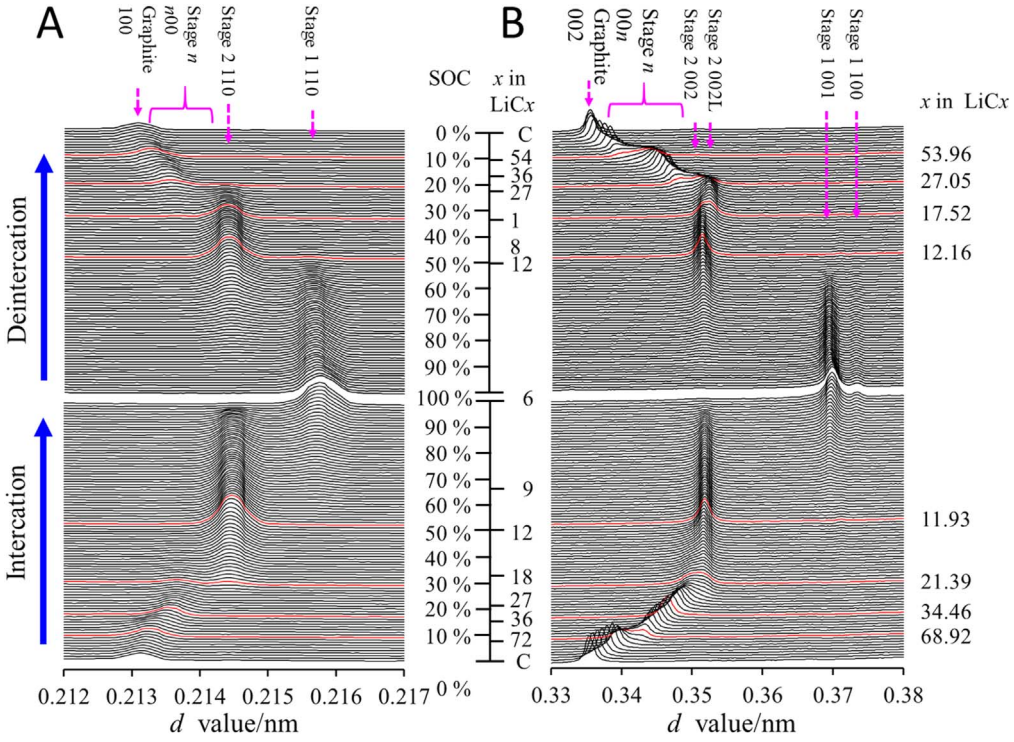

Figure 3. Variations in the patterns generated by the graphite electrodes, based on (A) (100) and (B) (002) reflections acquired during the intercalation/deintercalation processes.

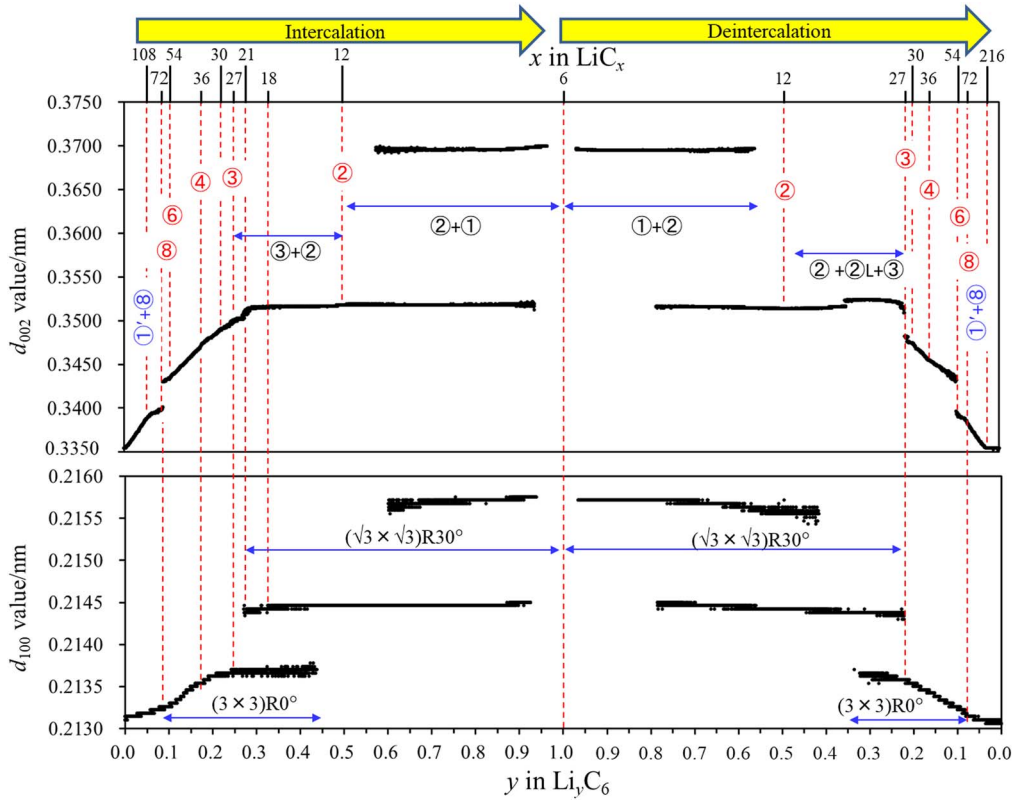

Figure 4. Changes in the Bragg values, *d*, for the (100) and (002) reflections of graphite. Values in circles denote the stage numbers.

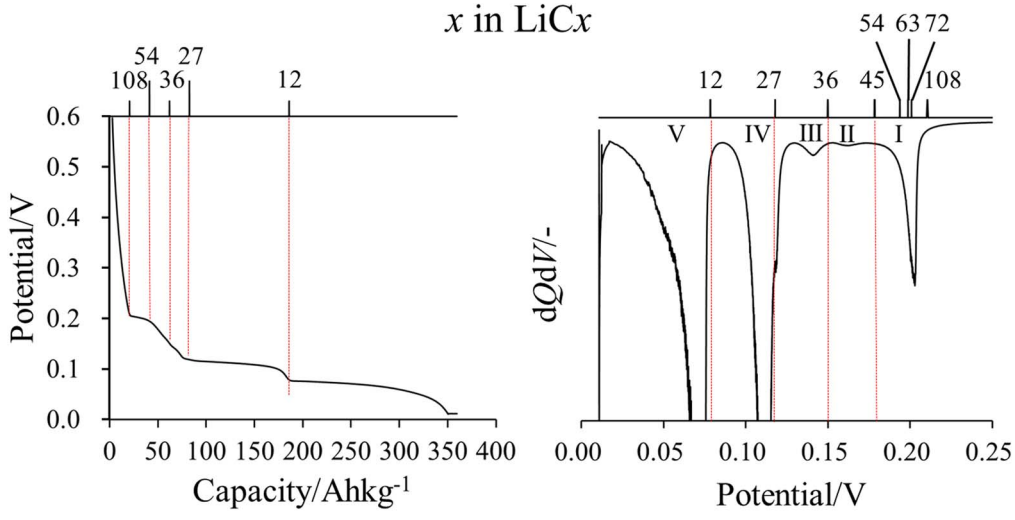

Figure 5. (A) Charge curve and (B) corresponding differential plot (*V*-d*Q*/d*V*).

Changes in the Graphite Stacking Sequence

Graphite is composed of thousands of graphene sheets stacked in an AB structure, while Li-GICs have AA stacking as shown in Fig. B·1. Consequently, as Li^+ intercalates/deintercalates into/from graphite, a transition between AB and AA stacking structures must take place at some point during the insertion and extraction processes. This transition is important in terms of clarifying the reaction mechanisms occurring at the graphite negative electrode. The changes in the 101 peak of the graphite, with a *d* value of approximately 0.2031 nm in Fig. 6A, can provide information concerning the stacking change, because this peak reflects the three-dimensional regularity peculiar to AB stacking. That is, the peak disappears after the transition from AB to AA induced by intercalation. Figure 6A summarizes the changes in the 101 and 002 peaks during the early stage of Li^+ insertion. Here, the broad peak at approximately 0.2031 nm represents the 101 peak while the peaks in the range of 0.202–0.203 nm are ascribed to the orientation due to microcrystals contained in non-uniform Al-laminate film. As the Li^+ insertion proceeded, the 101 peak gradually decreases in intensity and almost disappears over the compositional range of $LiC_{73.0}$–$LiC_{63.0}$. This finding provides clear evidence that the AB stacking of graphite was completely transformed to AA stacking in conjunction with Li^+ insertion at a composition of LiC_{63}. The disappearance of the 101 peak and the lack of any new diffraction peaks also indicate that the Li species were fully inserted into all the interlayers. This corresponds to the formation of a dilute stage 1 compound having a structure

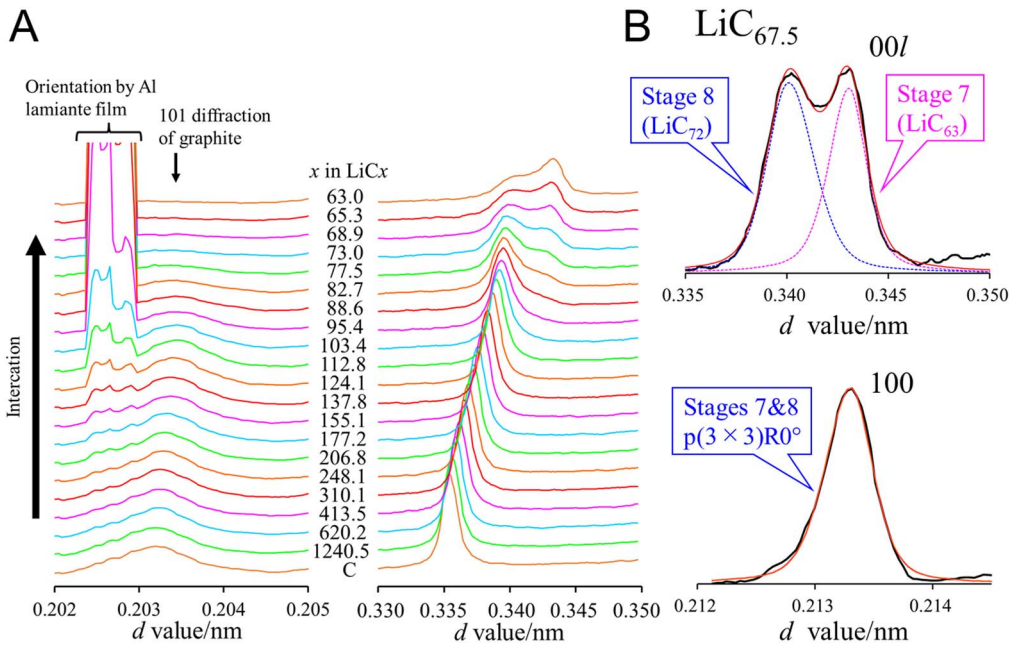

Figure 6. Diffraction patterns generated by graphite during the early stage of intercalation. Changes in (A) the 101 and 002 peaks and (B) the 100 and 00*l* peaks of $LiC_{67.5}$.

different from that of a typical LiC_6 stage 1 compound. Simultaneously, the 002 peak intensity decreases and the d_{002} value gradually increases from 0.335 to approximately 0.340 nm. The 002 peak eventually splits into a clear doublet in the compositional range of $LiC_{73.0}$–$LiC_{63.0}$, which demonstrates the formation of a new structure. As discussed above, Billaud et al. reported the formation of a p(3 × 3)R0°-type superlattice with the in-plane composition LiC_9.[8] Based on Billaud's work, the LiC_{63} and LiC_{72} Li-GICs are assigned to stages 7 and 8 with the same LiC_9-type in-plane structure, respectively. The changes in the 002 pattern during the early stage of insertion prior to the formation of the stage 8 compound is attributed to the formation and growth of the dilute stage 1 compound, followed by the transition from dilute stage 1 to stage 8 (LiC_{72}). As shown in Fig. 6B, the 002 pattern of the $LiC_{67.5}$, which is exactly intermediate between stages 7 and 8, contains two peaks with an almost 1:1 intensity ratio that indicates a 1:1 coexistence ratio. Because the atomic scattering factor of Li isso small, the structure factors of both stages are almost the same. The gradual change in the intensities of the peaks assigned to stages 8 and 7 confirm the coexistence of these two stages as the Li^+ is intercalated. This observation provides significant evidence for a LiC_9-type in-plane p(3 × 3)R0° structure for both stages. Consequently, it is not unexpected that the 100 pattern generated by the $LiC_{67.5}$ shows only a single peak at approximately 0.2133 nm (Fig. 6B). Figure 4 exhibits two vague inflection points at compositions LiC_{108} and LiC_{72} during intercalation. Similarly, Fig. 4 shows two inflection points associated with LiC_{216} and LiC_{72} during deintercalation The difference between Li^+ insertion and extraction produces very pronounced hysteresis between the intercalation and deintercalation processes within the region associated with low lithium contents.

Stage 2 and Dilute Stage 2 with a Larger d_{002} Value

The plots of *d* against *x* in Fig. 4 show a clear hysteresis between intercalation and deintercalation. Specifically, a new stage 2 with a larger d_{002} value appears in the composition range of LiC_{12}–LiC_{27} (see the 002 pattern in Fig. 3) during deintercalation. This compound was denoted as stage 2 l by Dahn, who found that this stage appeared during both intercalation and deintercalation.[6] Interestingly, the present *operando* study did not show evidence for a stage 2 l during the intercalation process (Figs. 7A and 1A). Figure 7 demonstrates that hysteresis also appeared between intercalation and deintercalation throughout stages 2–8. The changes in the peak positions and intensities over this range were different between intercalation and deintercalation. Notably, the change from stage 2 to stage 2 l during extraction increased the *d* value. The *d* value of the *a, b*-plane was unchanged during extraction. As the intensity of the 002 peak associated with stage 2 l increased, the intensity of the 110 peak decreased without a change in the *d* value, which indicates that stage 2 l likely represented a disturbance of the in-plane structure. Further, the peak at 0.216 nm attributed to the LiC_6 type in-plane structure of stage 1 was broader than that of stage 2 at 0.2145 nm. When a complete stage 1 with perfect composition of LiC_6 was formed, it should have a sharp peak, but with the graphite used in the present study, it reached to only $LiC_{6.2}$ even when fully charged. In other words, it is considered that the 110 peak is broad due to the partial presence of defects and the lack of a complete LiC_6 type in-plane structure. The Coulomb efficiency during charging and discharging is 99% or more, and in terms of X-ray diffraction, the 002 and 100 peaks have returned to their original diffraction positions, so basically the graphite have returned to the original graphite. However, since the 100 peak shape at ca.0.2132 nm after deintercalation is broadened in Fig. 7, there is a possibility that the graphene sheet is slightly distorted and 1% or less of Li ions remain between the interlayers.

Intercalation Pathway

Detailed analyses of the 002 and 100 peaks of graphite based on *operando* SXD established that various Li-GICs participate in the charge and discharge reactions at graphite negative electrodes in LIBs. Among these Li-GICs, those that appear in stages 1, 2 and 4 have been widely reported. The present results demonstrate the formation of LiC_{216}, LiC_{108}, LiC_{72}, LiC_{54}, LiC_{36}, LiC_{27}, LiC_{18}, LiC_{12} and LiC_6, although the diffractions of GICs formed at higher stages are not as clear. As discussed in the above sections, the p($\sqrt{3}$ × $\sqrt{3}$)R30° (in-plane LiC_6) and p(3 × 3)R0° (in-plane LiC_9) lattices play a role in the formation of Li-GICs during the charge and discharge of graphite negative electrodes in LIBs. However, the p($\sqrt{3}$ × $\sqrt{3}$)R30° structure appears only at a very high Li^+ concentration, that is, at a high SOC. The detailed analysis of patterns obtained from *operando* SXD, especially advanced assessment of the

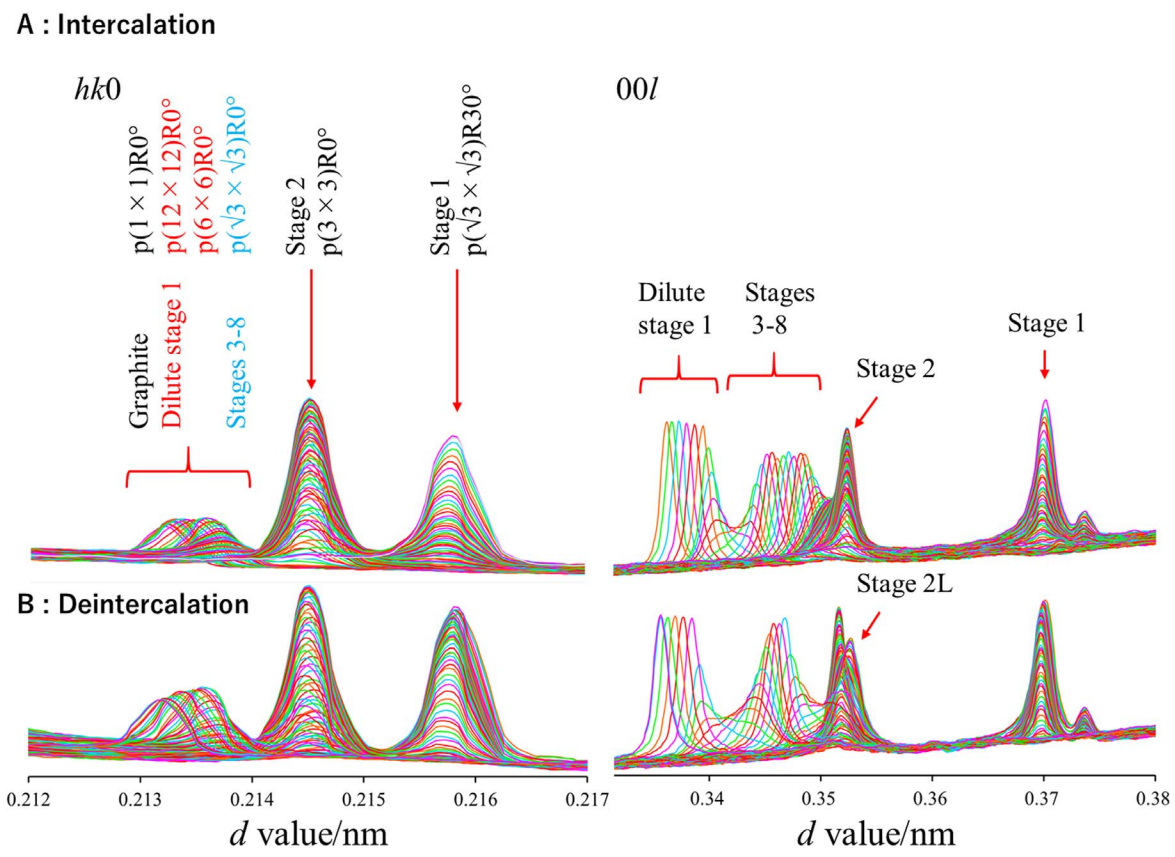

Figure 7. Superimposition of diffraction patterns acquired at 1% SOC increments during intercalation/deintercalation.

a, b-plane, indicates that the p(3 × 3)R0° unit lattice structure plays an important role in the generation of higher stage Li-GICs. Based on this, the p(6 × 6)R0° (LiC_{72}), p(6 × 12)R0° (LiC_{144}) and p(12 × 12)R0° (LiC_{288}) superlattice structures can be imaged, in addition to the p(3 × 3)R0° (LiC_{18}), p(√3 × √3)R30° (LiC_{12}) and p(√3 × √3)R30° (LiC_6) structures, as shown in Fig. 8. With the insertion of Li^+, the superlattice changes from dilute stage 1 with no *a,b*-plane structure to p(12 × 12)R0° (in-plane LiC_{288}), after which the latter undergoes stepwise changes through p(6 × 12)R0° (in-plane LiC_{144}), p(6 × 6)R0° (in-plane LiC_{72}) and p(3 × 3)R0° (in-plane LiC_{18}, LiC_9), and finally to p(√3 × √3)R30° (in-plane LiC_6). Because the lithium content is low up to p(3 × 3)R0°, it is typically difficult to obtain clear XRD patterns that can be ascribed to these structures, even using an SXD method. No clear signals attributable to p(6 × 6)R0° or p(12 × 12)R0° structures are observed before the appearance of LiC_{72}, and a jump in the d_{00l} value is evident at LiC_{72} in Fig. 4. The plots of the *d* values related to 100 peaks in Fig. 4 also indicate a clear inflection at this same Li-GIC. Thus, it appears that the LiC_{72} compound is associated with a transition from dilute stage 1 having a p(6 × 6)R0° in-plane structure before the jump to stage 8 with a p(3 × 3)R0° structure after the jump. With increases in the lithium insertion, a LiC_9-type in-plane structure was maintained up to stages 6, 5 and 4, at which point the LiC_{54}, LiC_{45} and LiC_{36} Li-GICs appeared, respectively. Figure 4 summarizes the consecutive changes in d_{00l} and d_{100} and indicates the difficulty in identifying LiC_{54}, LiC_{45} and LiC_{36}. On this basis, the diffraction data in Fig. 3 can be analyzed more carefully. Figure 9A shows the 100 and 00*l* patterns of the compounds having various low lithium contents. The d_{00l} patterns generated by the LiC_{72} and LiC_{63} contain two peaks corresponding to two different compositions. The d_{00l} peak data for LiC_{54} contain a tail at a smaller *d* value, which suggests that some LiC_{63} was present. The patterns related to the *a,b*-plane in Fig. 9A exhibit a shift from 0.2133 to 0.2137 nm with increasing Li content although this change is not stepwise but rather gradual. The Li concentrations were low in the Li-GICs associated with stages 8, 7 and 6 (equivalent to LiC_{72}, LiC_{63} and LiC_{54}) and so the total stabilization energy required to maintain each stage must have been low. Consequently, these stages should readily combine with neighboring stages. The patterns for the LiC_{45} and LiC_{36} compounds, both of which had intermediate lithium contents, contain sharper d_{00l} peaks and the variations in the peak positions are clearer. These results imply the formation of a product close to a single phase, consistent with the results of Billaud et al.[8] The d_{100} value for raw graphite, d^G_{100}, is geometrically related to the C–C bond length, d_{C-C}, through the equation $d_{C-C} = 2/3 \times d^G_{100}$. Therefore, the increase in *d* means that the size of the six-membered rings comprising the graphene sheets was increased as the lithium content increased.[34–37] The peaks related to the 100 peak *at* $d = 0.2136$ nm in Fig. 3A are seen to gradually decrease in intensity on going from stage 4 (LiC_{36}) to stage 3 (LiC_{27}). At a Li concentration higher than approximately LiC_{21-22}, another peak indexed as the 110 peak of the stage 2 compound appears at $d = 0.2146$ nm at lithium concentrations greater than approximately LiC_{21-22}. Corresponding changes in d_{00l} peaks are observed in Fig. 3, in which the 002 peak gradually shifts from $d = 0.346$ nm (stage 4, LiC_{36}) to larger values over the compositional range of LiC_{36}–LiC_{12}. In addition, at lithium concentrations exceeding the composition LiC_{27} (stage 3), the peak broadens and splits into a doublet then sharpens again and converges to $d = 0.352$ nm at the composition LiC_{12}. As noted briefly in the Introduction, stages 4 and 3 are equivalent to the p(3 × 3)R0° in-plane structure, while stage 2 has p(√3 × √3)R0° (LiC_{12}) and/or p(3 × 3)R0° (LiC_{18}) structures. Therefore, within this compositional range, a transition from stage 4 to stage 2 (LiC_{12}) via stage 3 (LiC_{27}) occurs along with a simultaneous in-plane transition from p(3 × 3)R0° to p(√3 × √3)R0°. Figure 9B provides the diffraction patterns of $LiC_{21.0}$ acquired along the in-plane and *c*-axis directions. Both patterns can be deconvoluted to give two peaks with an intensity ratio of about 1:1, which are assigned to the stage 3 and stage 2 compounds. Because stage 2 represents a mixture of LiC_{12} and LiC_{18}, its average composition is approximately LiC_{15}, while stage 3

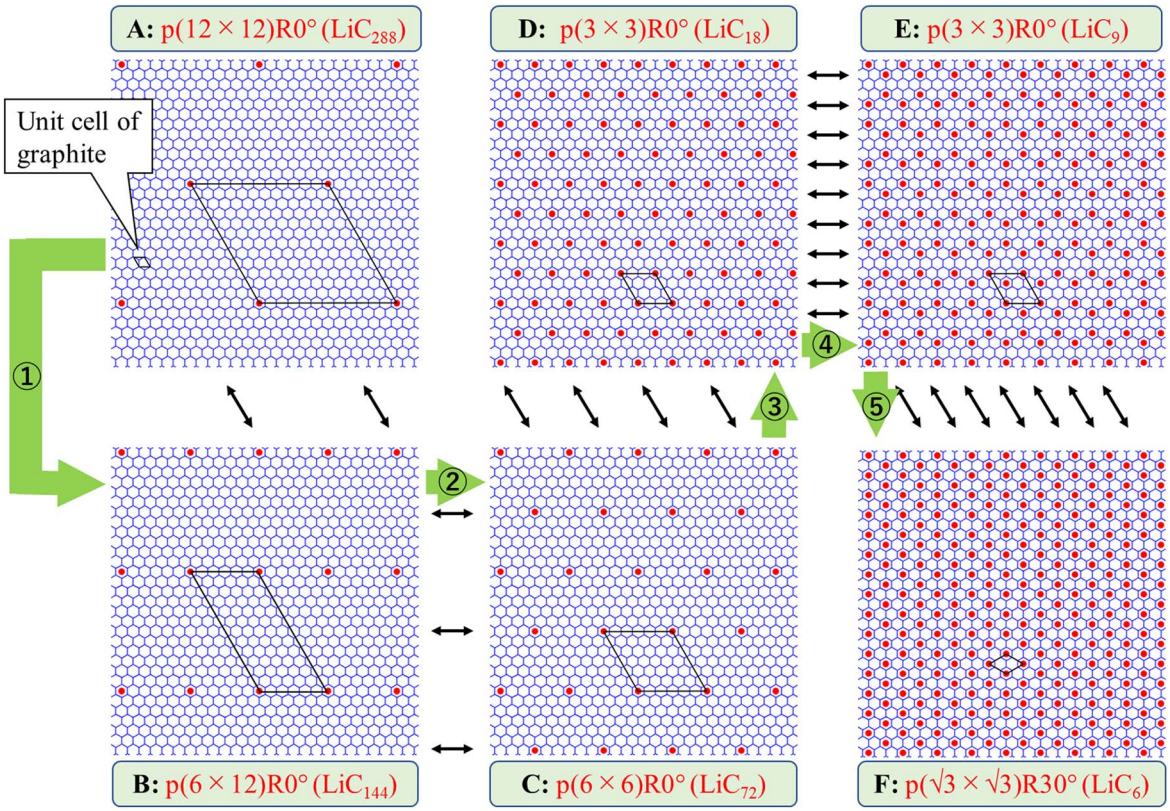

Figure 8. Schematic diagrams of rearrangements between possible superlattices in the order of A → B → C → D → E → F. The black arrow indicates the direction of movement of Li ions. The red circle represents the Li atom.

has the composition LiC_{27}. Thus, the mean composition of stages 3 and 2 is LiC_{21}, which explains the approximately 1:1 intensity ratio for these stages in the compositional range of LiC_{21}–LiC_{23}. Around this composition, the d_{100} value changes discontinuously and, at the same time, the intensity significantly decreases (as shown in Fig. 3A). The rearrangement from p(3 × 3)R0° to p(√3 × √3)R0° temporarily decreases the in-plane regularity of the superlattice. Consequently, the intensity of the 100 peak becomes weak in this compositional range and clear two-dimensional diffractions cannot be observed (see Fig. 3A). This in-plane rearrangement from p(3 × 3)R0° to p(√3 × √3)R0° also requires movement of Li^+ ions in the interlayers, which may cause torsion in the structure. In the compositional range of LiC_{12}–$LiC_{6.2}$ in Fig. 3, the peaks centered at 0.2145 and 0.2158 nm are attributed to the 110 peaks of the superlattices related to stages 2 and 1, respectively. In addition, the peaks at 0.352 and 0.370 nm are assigned to the 002 and 001 peaks of stages 2 and 1, respectively, and the 100 peak of stage 1 appears at 0.373 nm. These results demonstrate that the 110 and 100 peak intensities changed at the same time as the 00*l* peak intensity, and that the transition between stages occurred not only in the *c*-axis direction but also in the *a*, *b*-axial directions.

Deintercalation Pathway

The plot of *d* against *x* in Fig. 4 shows a clear hysteresis between intercalation and deintercalation. Specifically, a new stage 2 with a larger *d* value appears in the compositional range of LiC_{17}–LiC_{27} during deintercalation. This stage was denoted as stage 2 l by Dahn, who reported that both intercalation and deintercalation occurred in this stage.[15] However, in the present study, a 2 l stage is not observed during the intercalation process (Fig. 7). As the intensity of the 002 peak related to stage 2 l increases, the intensity of the 110 peak decreases. This result suggests that, during the stage 2 ↔ stage 2 l ↔ stage 3 transitions, the graphene sheets are subjected to a large strain and lose their regularity. This strain leads to expansion in the direction of the *c*-axis and to increases in the interlayer spacing. The structure of the stage 2 l thus appears to represent a transition from p(√3 × √3)R30° to p(3 × 3)R0°.

Conclusions

Plots of the *d* values as a function of *x* demonstrated several inflection points and jumps at the compositions LiC_{6n}, LiC_{9n} and LiC_{72n}. These results suggested the dynamic formation of three new in-plane superlattices during charge/discharge: LiC_{288} (p(12 × 12)R0°), LiC_{144} (p(6 × 12)R0°) and LiC_{72} (p(6 × 6)R0°). During the initial stage of intercalation, Li^+ ions were inserted into all the interlayers with equal probability, and so were randomly situated within the interlayers. Consequently, the conjugated π-electron system in the graphene was disturbed and a dilute stage 1 compound was formed. As increasing amounts of Li^+ were incorporated, these ions were rearranged in the interlayers and an in-plane superlattice structure was formed in each layer to stabilize the conjugated system in the carbon network. A LiC_{288} superlattice (p(12 × 12)R0°) appears to have initially formed, and increasing insertion of Li^+ produced LiC_{72} (p(6 × 6)R0°) via LiC_{144} (p(6 × 12)R0°). Prior to the formation of LiC_{72}, the disturbed conjugated π-electron system in the graphene (meaning the dilute stage 1 structure) was maintained. When the Li^+ concentration produced LiC_{72}, stabilization of the entire system having a dilute stage 1 structure became difficult. A structural change occurred in the direction of the *c*-axis to form the new stage 8 material having the composition LiC_{72} via rearrangement of the in-plane structure from LiC_{72} (p(6 × 6)R0°, dilute stage 1) to LiC_9 (p(3 × 3)R0°, stage 8). Beyond LiC_{72}, consistent with the Daumas–Hérold model,[38–40] the stage transition proceeded in the order of 8 → 7 → 6 → 5 → 4 → 3 → 2, which maintained the in-plane LiC_9 (p(3 × 3)R0°) structure. With further intercalation of Li^+, the LiC_9 in-plane structure could no longer be

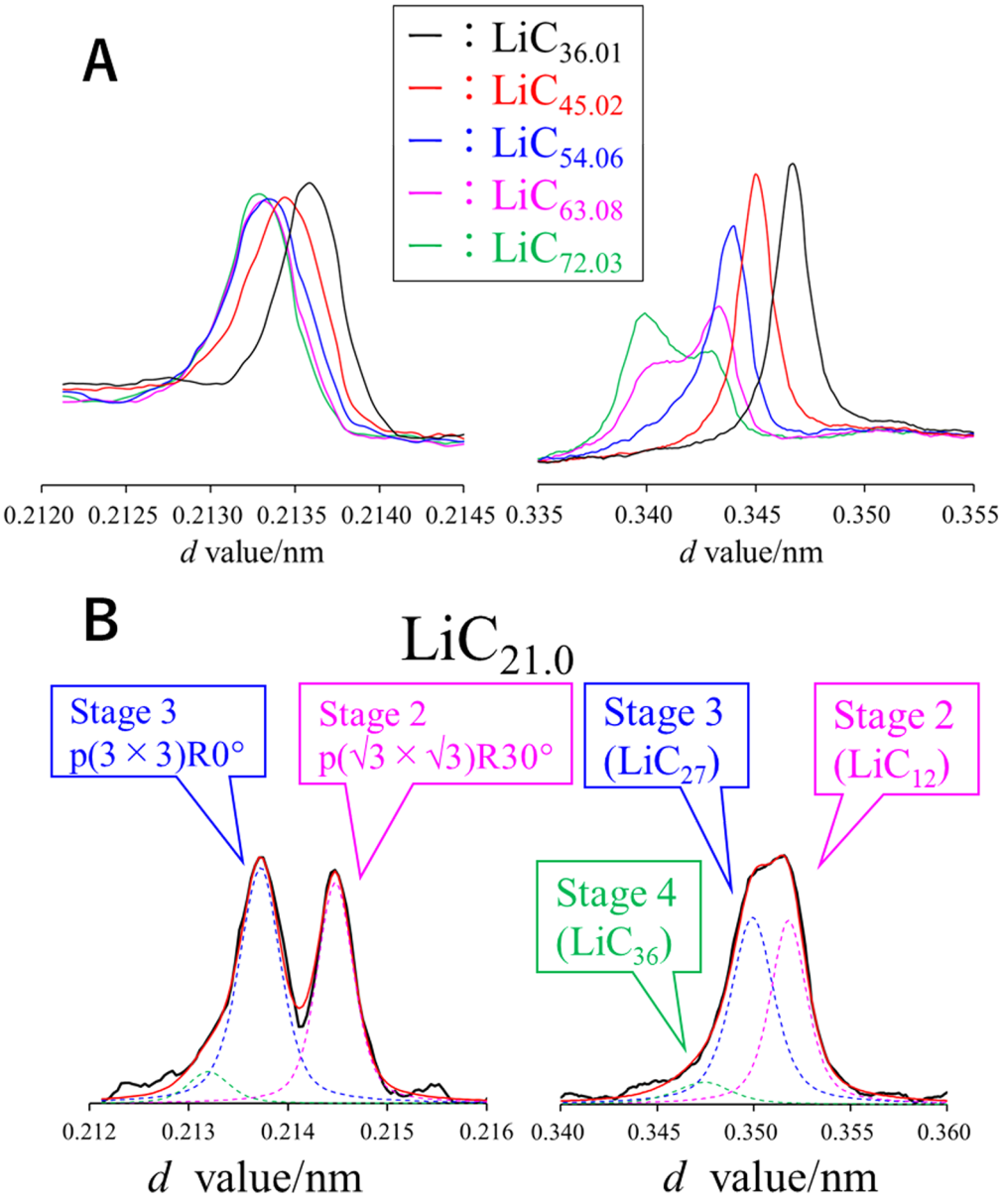

Figure 9. Changes in the 100, 101 and 002 peaks of graphite. (A) The 100 and 00*l* peaks of LiC_{9n} (n = 4–8) and (B) the 100 and 00*l* peaks of $LiC_{21.0}$.

maintained and the rearrangement from LiC_9 (p(3 × 3)R0°) to LiC_6 (p(√3 × √3)R0°) took place while maintaining the stage 2 structure. With increases in the Li^+ insertion, stage 2 finally transitioned to the LiC_6 in-plane structure. The stage 2 (p(√3 × √3)R0°) structure then changed to stage 1, having the same in-plane structure, with increasing Li^+ insertion. This series of structural changes both homogenized and stabilized the conjugated π-electron system in the graphene network through the exchange of electrons between the Li^+ ions and graphite. With sufficient Li insertion, multiple rearrangements of the superlattice could occur. As a result, the above transition through successive stages also proceeded in the *c*-axis direction of the stacked graphene sheets, although this was not the dominant process in this direction. Graphite has such a strong anisotropy along the *c*-axis that these in-plane structural changes have not previously been detected. Thus, the most important aspect of this study is the demonstration of a technique to track successive changes in the in-plane diffraction patterns of graphene. On the basis of the above findings, intercalation can be understood as a reaction in which the intercalant forms an in-plane superlattice structure between the interlayers to delocalize the electrons and stabilize the conjugated π-electron system. The resulting superlattice can undergo repeated rearrangement, changing its size and shape, depending on the amount of intercalant.

Acknowledgments

This work was supported by the Research and Development Initiative for Scientific Innovation of New Generation Batteries 2 (RISING2) project and the New Energy and Industrial Technology Development Organization (NEDO). The synchrotron X-ray diffraction experiments were performed on the BL28XU beamline at the SPring-8 facility with the approval of the Japan Synchrotron Radiation Research Institute (JASRI) (proposal nos. 2016A7602, 2016B7603, 2017A7603, 2017B7603, 2018A7603, 2019A7613 and 2019B7613). We thank Michael D. Judge, MSc, from Edanz Group (https://en-author-services.edanzgroup.com/ac) for editing a draft of this manuscript.

Appendix A

A.1. Crystallography of in-plane superlattices and 00n diffractions of stage n compounds.—Li intercalation between graphite layers increases the interlayer distance, such that the 002 peak of the graphite continuously shifts to the lower diffraction angle in association with

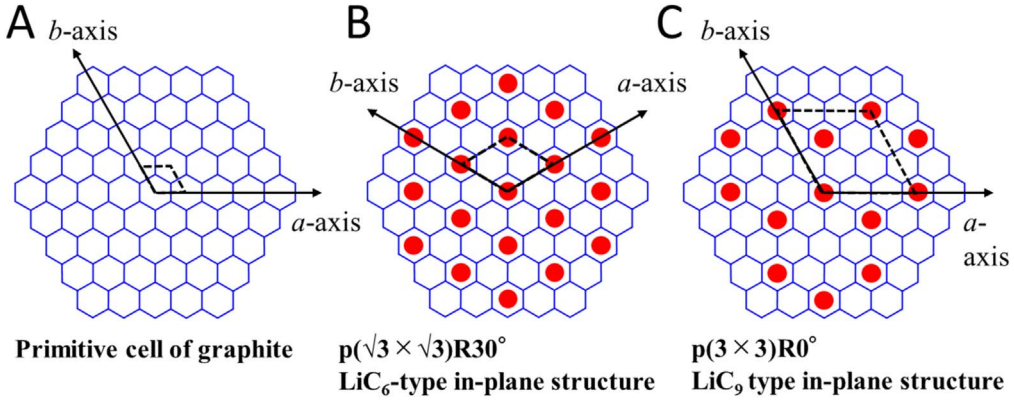

Figure A·1. Schematic diagrams of the unit cells of (A) graphite, (B) a LiC_6-type in-plane superlattice, and (C) a LiC_9-type in-plane superlattice.

Table A·I. Bragg values (d) of various superlattices.

	Graphite	LiC_6	LiC_9	LiC_{72}	LiC_{288}
Type of Superlattice	p(1 × 1)R0°	p(√3 × √3)R30°	p(3 × 3)R0°	p(6 × 6)R0°	p(12 × 12)R0°
a_0/nm	$a^G_0 = 0.24612$	$\sqrt{3}a^G_0 = 0.42629$	$3a^G_0 = 0.73836$	$6a^G_0 = 1.47672$	$12a^G_0 = 2.95344$
d_{100}/nm ($\sqrt{3}a_0/2$)	**0.21315**	0.36919	0.63945	1.2789	2.5578
d_{110}/nm ($a_0/2$)	0.12306	**0.21315**	0.36919	0.73836	1.47672
d_{200}/nm ($\sqrt{3}a_0/4$)	0.10657	0.18458	0.31917	0.63945	1.2789
d_{300}/nm ($\sqrt{3}a_0/6$)	0.07105	0.12306	**0.21315**	0.4263	0.8526
d_{600}/nm ($\sqrt{3}a_0/12$)	—	—	—	**0.21315**	—
d_{1200}/nm ($\sqrt{3}a_0/24$)	—	—	—	—	**0.21315**

increasing d values. Therefore, when stage n appears, the 002 peak of graphite becomes the 00n peak. In the present paper, even in the case that a line is attributed to the d_{00n} peak of a stage n compound, this may in fact described as the d_{002} peak of graphite.

Two types of structures have been proposed for Li-graphite intercalation compounds (Li-GICs): p(√3 × √3)R30° and p(3 × 3)R0° (Fig. A·1). In the notation used for these in-plane structures, p denotes a primitive unit cell, ($i \times j$) denotes the unit vectors measured in units of $a_0 = 0.24612$ nm in the hexagonal lattice primitive cell, and Rθ denotes the angle of rotation of the unit vectors of the lattice relative to the graphite unit vectors. The p($i \times i$) superlattice structure is obtained by repeating the unit cell of graphite i-fold along both the a and b axes. The d_{m00} value of a p($m \times m$)R0°-type superlattice (m = 3, 6, 12 but not √3) is crystallographically equivalent to the d^G_{100} value (0.21315 nm) of the graphite unit cell, and so these two reflections cannot be differentiated. Similarly, the d_{110} value of a p(√3 × √3)R30° structure is identical to the d^G_{100} of graphite. Hence, the 100 peaks of graphite that were assessed in the work presented herein were equivalent to the d_{m00} or d_{110} values of the superlattices. Consequently, in the present paper, even if a peak is referred to as the d_{100} line of graphite, it may refer to the d_{m00} or d_{110} peaks of the superlattice. In addition, the d^G_{100} value is geometrically related to the C–C bond length, $d_{C–C}$, via the equation $d_{C–C} = 2/3 \times d^G_{100}$, as shown in Table A·I. Hence, we were able to estimate variations in the size of the six-membered carbon rings in the graphite from changes in the d_{100} value.

Appendix B

B.1. Li-GIC and graphite stacking sequences.—Graphite has an AB stacking structure while Li-GICs have AA stacking. Hence, when Li ions intercalate/deintercalate into/from graphite, a transition from AB to AA or from AA to AB stacking must occur at some point in the process, and this is very important when analyzing the reaction mechanism. In both of the stacking structures, the (101) reflection has a geometrical configuration as shown in Fig. B·1

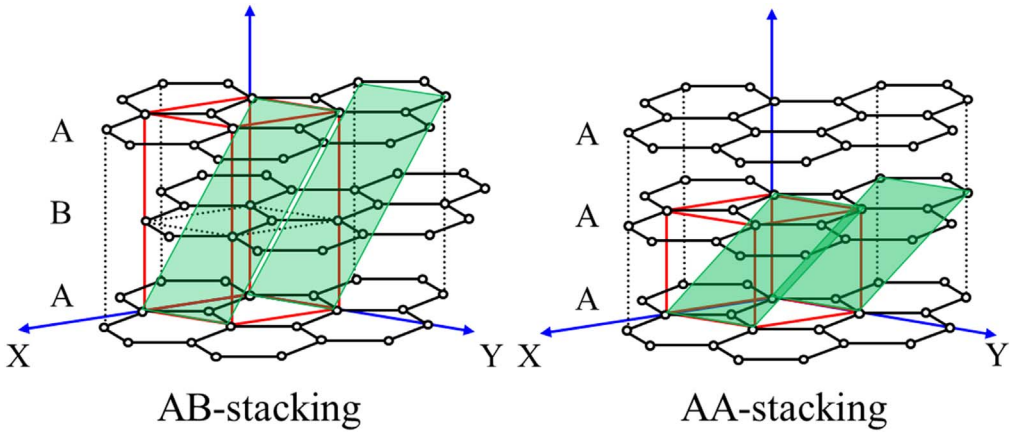

Figure B·1. Possible graphite stacking sequences. Green planes denote the (101) reflection planes.

(green plane), so there is a difference in the Bragg's d spacing value between the both. This reflection is related to the three-dimensional regularity peculiar to the stacking structure, and the 101 diffraction of graphite disappears when the transition from AB to AA occurs. To assess this phenomenon, variations in 101 peaks based on the d_{101} value of approximately 0.2031 nm for graphite were monitored.

ORCID

Hiroyuki Fujimoto https://orcid.org/0000-0003-4562-7715
Ken-ichi Okazaki https://orcid.org/0000-0003-0800-712X

References

1. A. Hérold, *Bull. Soc. Chim. France*, **187**, 999 (1955).
2. D. Guerard and A. Hérold, *Carbon*, **13**, 337 (1975).
3. D. Guerard, M. Chaabouni, P. Lagrange, M. E. Makrini, and A. Hérold, *Carbon*, **18**, 257 (1980).
4. N. Kambe, M. S. Dresselhaus, G. Dresselhaus, S. Basu, A. R. McGhie, and J. E. Fischer, *Mat. Sci. Eng.*, **40**, 1 (1979).
5. M. S. Dresselhaus and G. Dresselhaus, *Adv. Phys.*, **30**, 139 (1981).
6. N. Emery, C. Hérold, and P. Lagrange, *Prog. Solid State Chem.*, **36**, 213 (2008).
7. S. Basu, C. Zeller, P. J. Flanders, C. D. Fuerst, W. D. Johnson, and J. E. Fischer, *Mat. Sci. Eng.*, **38**, 275 (1979).
8. D. Billaud, E. McRae, J. F. Mareche, and A. Hérold, *Synth. Met.*, **3**, 21 (1981).
9. S. B. Dicenzo, S. Basu, and G. K. Werthem, *Synth. Met.*, **3**, 139 (1981).
10. P. Pfluger, V. Geiser, S. Stolz, and H.-J. Güntherodt, *Synth. Met.*, **3**, 27 (1981).
11. J. R. Dahn, *Phys. Rev. B*, **44**, 9170 (1991).
12. M. Inaba, H. Yoshida, Z. Ogumi, T. Abe, Y. Mizutani, and M. Asano, *J. Electrochem.*, **142**, 20 (1995).
13. R. Yazami and Y. Reynier, *J. Power Sources,*, **153**, 312 (2006).
14. M. Letellier, F. Chevallier, and M. Morcrette, *Carbon*, **45**, 1025 (2007).
15. F. Chevallier, F. Poli, B. Montigny, and M. Letellier, *Carbon*, **61**, 140 (2013).
16. T. Ohzuku, Y. Iwakoshi, and K. Sawai, *J. Electrochem. Soc.*, **140**, 2490 (1993).
17. K. Zaghib, K. Tatsumi, Y. Sawada, S. Higuchi, H. Abe, and T. Ohsaki, *J. Electrochem. Soc.*, **146**, 2784 (1999).
18. S. A. Krachkovskiy, J. M. Foster, J. D. Bazak, B. J. Balcom, and G. R. Goward, *J. Phys. Chem. C*, **122**, 21784 (2018).
19. A. I. Freytag, A. D. Pauric, S. A. Krachkovskiy, and G. R. Goward, *J.Am.Chem. Soc.*, **141**, 13758 (2019).
20. S. Schweidler, L. Biasi, A. Schiele, P. Hartmann, T. Brezesinski, and J. Janek, *J. Phys. Chem. C*, **122**, 8829 (2018).
21. A. Senyshyn, M. J. Mühlbauer, K. Nikolowski, T. Pirling, and H. Ehrenberg, *J. Power Sources,*, **203**, 126 (2012).
22. A. Senyshyn, O. Dolotko, M. J. Mühlbauer, K. Nikolowski, H. Fuess, and H. Ehrenberg, *J. Electrochem. Soc.*, **160**, A3198 (2013).
23. H. He, C. Huang, C. W. Luo, J. J. Liu, and Z. S. Chao, *Electrochim. Acta*, **92**, 148 (2013).
24. N. Sharma and V. K. Peterson, *Electrochim. Acta*, **101**, 79 (2013).
25. L. Cai, K. An, Z. Feng, C. Liang, and S. J. Harris, *J. Power Sources,*, **236**, 163 (2013).
26. N. Sharma and V. K. Peterson, *J. Power Sources,*, **244**, 695 (2013).
27. O. Dolotko, A. Senyshyn, M. J. Mühlbauer, K. Nikolowski, and H. Ehrenberg, *J. Power Sources,*, **255**, 197 (2014).
28. V. Zinth, C. Lüders, M. Hofmann, J. Hattendorff, I. Buchberger, S. Erhard, J. R. Kornmeier, A. Jossen, and R. Gilles, *J. Power Sources,*, **271**, 152 (2014).
29. H. Park, M. Kim, F. Xu, C. Jung, S. M. Hong, and C. M. Koo, *J. Power Sources,*, **283**, 68 (2015).
30. N. A. Canas, P. Einsiedel, O. T. Freitag, C. Heim, M. Steinhauer, D. W. Park, and K. A. Friedrich, *Carbon*, **116**, 255 (2017).
31. T. Matsunaga, S. Takagi, K. Shimoda, K. Okazaki, Y. Ishikawa, M. Yonemura, Y. Ukyo, T. Fukunaga, and E. Matsubara, *Carbon*, **142**, 513 (2019).
32. J. K. Mathiesen, R. E. Johnsen, A. S. Blennow, and P. Norby, *Carbon*, **153**, 347 (2019).
33. H. Li, S. Guo, and H. Zhou, *J. Ener. Chem*, **59**, 191 (2021).
34. D. E. Nixon and G. S. Parry, *J. Phys. C: Solid State Phys.*, **2**, 1732 (1969).
35. L. Pietronero and S. Strässler, *Phys. Rev. Lett.*, **47**, 593 (1981).
36. C. T. Chan, W. A. Kamitakahara, and K. M. Ho, *Phys. Rev. Lett.*, **58**, 1528 (1987).
37. C. T. Chan, K. M. Ho, and W. A. Kamitakahara, *Phys. Rev. B*, **36**, 3499 (1987).
38. N. Daumas and A. Hérold, *C. R. Acad. Sci. Ser. C*, **268**, 373 (1969).
39. S. Krishnan, G. Brenet, E. M. Charry, D. Caliste, L. Genovese, T. Deutsch, and P. Pochet, *Appl. Phys. Lett.*, **103**, 251904 (2013).
40. E. M. G. Arriazu, O. A. Pinto, B. A. L. Mishima, D. E. Barraco, O. A. Oviedo, and E. P. M. Leiva, *Electrochem. Commun.*, **93**, 133 (2018).